



Title	The occurrence of cirrus clouds associated with eastward propagating equatorial $n = 0$ inertio-gravity and Kelvin waves in November 2011 during the CINDY2011/DYNAMO campaign
Author(s)	Suzuki, Junko; Fujiwara, Masatomo; Nishizawa, Tomoaki; Shirooka, Ryuichi; Yoneyama, Kunio; Katsumata, Masaki; Matsui, Ichiro; Sugimoto, Nobuo
Citation	Journal of Geophysical Research: Atmospheres, 118(23), 12,941-12,947 https://doi.org/10.1002/2013JD019960
Issue Date	2013-12-16
Doc URL	http://hdl.handle.net/2115/64741
Rights	Copyright 2013 American Geophysical Union.
Type	article
File Information	Suzuki_et_al-2013-Journal_of_Geophysical_Research__Atmospheres.pdf



[Instructions for use](#)

The occurrence of cirrus clouds associated with eastward propagating equatorial $n=0$ inertio-gravity and Kelvin waves in November 2011 during the CINDY2011/DYNAMO campaign

Junko Suzuki,¹ Masatomo Fujiwara,² Tomoaki Nishizawa,³ Ryuichi Shirooka,¹ Kunio Yoneyama,¹ Masaki Katsumata,¹ Ichiro Matsui,³ and Nobuo Sugimoto³

Received 17 April 2013; revised 14 October 2013; accepted 11 November 2013; published 9 December 2013.

[1] Cirrus cloud variability associated with $n=0$ eastward inertio-gravity equatorial waves and equatorial Kelvin waves (both with the period of ~ 4 days) and equatorial Kelvin wave with another periodicity (~ 16 days) were observed in the tropical Indian Ocean (8.0°S , 80.5°E) in November of 2011 during the Cooperative Indian Ocean experiment on intraseasonal variability in the Year 2011 (CINDY2011)/Dynamics of the Madden-Julian Oscillation (DYNAMO) field campaign using balloon-borne cryogenic frostpoint hygrometers, Vaisala radiosondes, and a shipborne high spectral resolution lidar system. During early to mid-November, the cirrus cloud appearance corresponded primarily with high supersaturation and high relative humidity caused by the temperature disturbances associated with the ~ 4 day waves between 12 km altitude and the cold-point tropopause. The cirrus clouds disappeared under the unfavorable (downward wind and dry) conditions that were caused by the ~ 4 day waves, although the ~ 16 day wave was generating favorable conditions. Our multi-instrument cirrus measurements revealed that we must consider the phases of various overlapping waves when estimating dehydration efficiency caused by cirrus clouds around the cold-point tropopause.

Citation: Suzuki, J., M. Fujiwara, T. Nishizawa, R. Shirooka, K. Yoneyama, M. Katsumata, I. Matsui, and N. Sugimoto (2013), The occurrence of cirrus clouds associated with eastward propagating equatorial $n=0$ inertio-gravity and Kelvin waves in November 2011 during the CINDY2011/DYNAMO campaign, *J. Geophys. Res. Atmos.*, 118, 12,941–12,947, doi:10.1002/2013JD019960.

1. Introduction

[2] Cirrus clouds frequently occur in the tropical tropopause layer (TTL) and play a critical role in the dehydration mechanisms of air entering the stratosphere [Holton and Gettelman, 2001; Fueglistaler et al., 2009]. The dehydration processes in the TTL control water vapor variability in the lower stratosphere and may influence surface temperatures through their impact on the global distribution of the radiation budget [Solomon et al., 2010]. The variability of cirrus clouds in the TTL is dependent on cloud microphysics, cloud dynamics, and large-scale dynamics.

[3] Various atmospheric waves around the TTL could determine the conditions for cirrus cloud generation and maintenance by perturbing the temperature field and controlling the horizontal and vertical motions [e.g., Jensen and Pfister, 2004]. Several observational studies have reported that equatorial Kelvin waves and the Madden-Julian Oscillation (MJO), the two dominant disturbances in the

TTL, cause cirrus variability and determine global cirrus distribution [Boehm and Verlinde, 2000; Eguchi and Shiotani, 2004; Fujiwara et al., 2009; Virts et al., 2010; Suzuki et al., 2010a; Inai et al., 2012]. On shorter scales, Pfister et al. [2001] used the aircraft-borne lidar data near the tropical tropopause to demonstrate that gravity waves contribute to the formation of cirrus clouds. Although there are a variety of types of equatorial waves in the TTL, in addition to Kelvin waves [e.g., Matsuno, 1966], their impact on cirrus variability remains unclear.

[4] In this paper, we investigate cirrus variations associated with two types of equatorial waves over the tropical Indian Ocean (8.0°S , 80.5°E) in November of 2011. This study mainly utilizes data from the Cooperative Indian Ocean experiment on intraseasonal variability in the Year 2011 (CINDY2011)/Dynamics of the Madden-Julian Oscillation (DYNAMO) field campaign [Yoneyama et al., 2013]. In this campaign, we conducted regular radiosoundings at 3 h intervals, 15 balloon-borne cryogenic frostpoint hygrometer (CFH) soundings, and continuous high spectral resolution lidar (HSRL) measurements on board the research vessel (R/V) *Mirai*. After describing the cirrus variability over the vessel during the study period, we investigate the humidity and temperature conditions inside the cirrus. We then characterize the equatorial waves that modulate this cirrus variability.

2. Data and Methodology

[5] During the CINDY2011/DYNAMO field campaign lasting from late September of 2011 to early January of

¹Japan Agency for Marine-Earth Science and Technology, Yokosuka, Japan.

²Graduate School of Environmental Science, Hokkaido University, Sapporo, Japan.

³National Institute for Environmental Studies, Tsukuba, Japan.

Corresponding author: J. Suzuki, Research Institute for Global Change, Japan Agency for Marine-Earth Science and Technology, Natsushima 2-15, Yokosuka 237-0061, Japan. (suzukij@jamstec.go.jp)

2012, the R/V *Mirai* sailed in the tropical Indian Ocean with a primary objective of studying the initiation of the MJO; the ship remained at 8.0°S, 80.5°E from 30 September to 24 October and from 31 October to 28 November [Yoneyama *et al.*, 2013; see the R/V *Mirai*'s track in their Figure 4]. On board the vessel, Vaisala RS92 radiosondes were regularly launched at 3 h intervals, and a total of 15 cryogenic frostpoint hygrometers (CFHs) [Vömel *et al.*, 2007] were launched. The CFH is a chilled mirror hygrometer which can measure the temperature of a frost layer on a small mirror that is kept in equilibrium with the atmospheric water vapor; this temperature is by definition called the frostpoint temperature. The relative humidity over ice (RH_i) in the upper troposphere was calculated with the frostpoint temperature measured using the CFHs and with the air temperature measured using the Meisei RS06G radiosonde that was attached directly to each CFH. The accuracy of the troposphere (stratosphere) measurements is better than 5% (10%) RH_i [Vömel *et al.*, 2007]. The Meisei RS06G radiosonde transmitted the CFH and radiosonde data every 1 s. Because the ascending speed of the balloon was set at $\sim 5 \text{ m s}^{-1}$, the corresponding vertical resolution of the data was $\sim 5 \text{ m}$. In this paper, we averaged the data for each 100 m bin to improve its statistical interpretation.

[6] Also, we continuously operated the high spectral resolution lidar (HSRL) instrument of the National Institute for Environmental Studies (Japan) on board the vessel. The lidar system separately measures signals at 532 nm that are backscattered by atmospheric particles and molecules using a HSRL technique that is different from the conventional Mie scattering lidar; the HSRL method directly provides particle backscatter and extinction coefficients at 532 nm for optically thick aerosols and clouds without assuming a lidar ratio [Nishizawa *et al.*, 2010, 2012]. The HSRL system also provides attenuated backscatter coefficients at 1064 nm (P_{1064}).

[7] The P_{1064} data for the total (atmospheric particle and molecule) scattering were originally provided at 1 min temporal and 3.75 m vertical resolutions. Here we averaged at every 60 min intervals and for 90 m vertically to compare the RH_i profiles measured by the CFHs and to reduce random noise. We used a threshold of 6.2×10^{-5} (~ -4.2 in the common logarithm) $\text{km}^{-1} \text{sr}^{-1}$ to keep cloud signals by comparing to the RH_i profiles (see section 3 for details). To detect cloud layers and to calculate the optical depth for every cloud at each time point, three criteria for spatial homogeneity were applied. Note that observed clouds were judged as nonspherical ice clouds if they have both adequate P_{1064} and particle extinction (β_{532}) signals by following the below mentioned methodology: First, a cloud layer must have had vertically consecutive P_{1064} signals over the threshold for at least 180 m; thus, the vertical distance between cloud layers must have been equal to or greater than 180 m. Second, clouds whose base was lower than 6 km ($\sim -0^\circ\text{C}$) were removed from this study because we focused on ice clouds only. Third, the optical depth (τ) was estimated by integrating β_{532} for each cloud layer. It is often difficult to clearly measure the signal-to-noise ratio of β_{532} for the subvisible cirrus (SVC) clouds, which are identified by their very low optical depth [Kärcher, 2002]; therefore, we estimated the SVC optical depth by integrating the particle backscatter at 532 nm using a lidar ratio of $S=25$ [cf. Martins *et al.*, 2011]. We

defined the SVC as a cloud layer with an optical depth of $\tau < 0.03$ [cf. Sassen and Cho, 1992] and a cloud base of $>10 \text{ km}$. The HSRL ground-based observation system was capable of observing cloud particles up to the cold-point tropopause every day without being obstructed by thick clouds in the lower troposphere during the second observation period (from 31 October to 27 November), as discussed in section 3. We also used hourly surface rainfall obtained on board the vessel.

[8] To investigate the relationship between the cirrus variability and large-scale disturbances, we analyzed the temperature, zonal wind, meridional wind, and geopotential height data at 125 hPa ($\sim 15.3 \text{ km}$) and 100 hPa ($\sim 16.5 \text{ km}$) obtained from the European Centre for the Medium-Range Weather Forecasts Re-Analysis (ERA-Interim) data [Dee *et al.*, 2011], which are produced every 6 h and gridded at 1.5° in both longitude and latitude.

3. Results and Discussion

[9] Figure 1 shows the time-altitude distribution of the 1064 nm attenuated backscatter coefficient (P_{1064}) for cirrus cloud signals over the R/V *Mirai*. During the study period, cirrus clouds were continuously observed at altitudes from 12 km to the cold-point tropopause. The tops of these clouds frequently reached the cold-point tropopause, which fluctuated every several days. It was observed that a very low cold-point tropopause was often associated with the top of high cirrus layers. SVC ($\tau < 0.03$) frequently appeared at 14–16 km and both above and below thick cirrus clouds; on the other hand, there were no thick clouds in the vicinity (e.g., in 8 November at ~ 14 – 15 km).

[10] The Madden-Julian Oscillation Index (i.e., the MJO index), as defined by Wheeler and Hendon [2004], is used to represent the time-varying phase of the MJO. As shown in Figure 1, all of the MJO phases (MJO index 1–8) occurred in the observation period; the active convection center of the MJO was located over the equatorial Indian Ocean during phases 2 and 3, over the Indonesian maritime continent during phases 4 and 5, over the western Pacific during phases 6 and 7, and in the Western Hemisphere and over equatorial Africa during phases 8 and 1. Convective system of the MJO was reached in phase 3 over the equatorial Indian Ocean in 25 November. The HSRL system was able to observe cirrus clouds as far as the cold-point tropopause with exception of a few hours when precipitation occurred. The system provided 60 min period interval data until 26 November. The appearance frequency (%) for each day was defined as $T_{\text{cloud}}/T_{\text{norain}}$, where T_{cloud} was cloud appearance time (hours) and T_{norain} was no rain time (hours). Note that the precipitation durations were less than or equal to 40 min (not shown) and total precipitation time was 370 min (0.99%) during 1–26 November. This information was obtained from the 10 min interval rain gauge data. The cloud appearance frequency (in a day) over the vessel decreased during phase 4, which is consistent with a previous study that showed using Cloud-Aerosol Lidar and Infrared Pathfinder Satellite Observations data that cirrus signals over the Indian Ocean weakened during phases 4 and 5 [e.g., Virts *et al.*, 2010]. However, in other phases, cloud appearance was subject to frequent fluctuations, even in the same MJO phase. The variability in cloud appearance frequency for both total cirrus

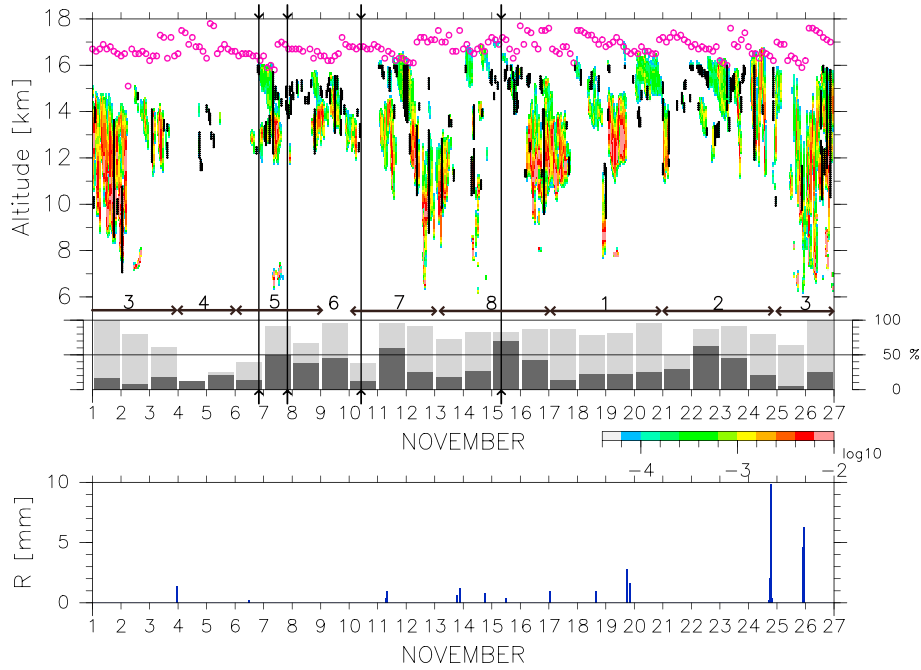


Figure 1. (top) Time-altitude distribution of the 1064 nm attenuated backscatter coefficient (P_{1064}) for the cirrus signals at 6–18 km over the R/V *Mirai* during the period of 1–26 November 2011. Regions with $\geq 6.2 \times 10^{-5} \text{ km}^{-1} \text{ sr}^{-1}$ are colored. The location of SVC clouds ($\tau < 0.03$) is indicated by black dots on the colored cloud signals. The purple circles denote the location of the cold-point tropopause. Gray-colored bars at the bottom indicate the cloud appearance frequency (%) for each day; darker bars are for SVC clouds only. The numbers (1–8) indicate the phase of the MJO index (see text for details). Vertical lines denote the times of the CFH launches corresponding to results shown in Figure 2. (bottom) Hourly surface rainfall at the R/V *Mirai* during the period of 1–26 November 2011.

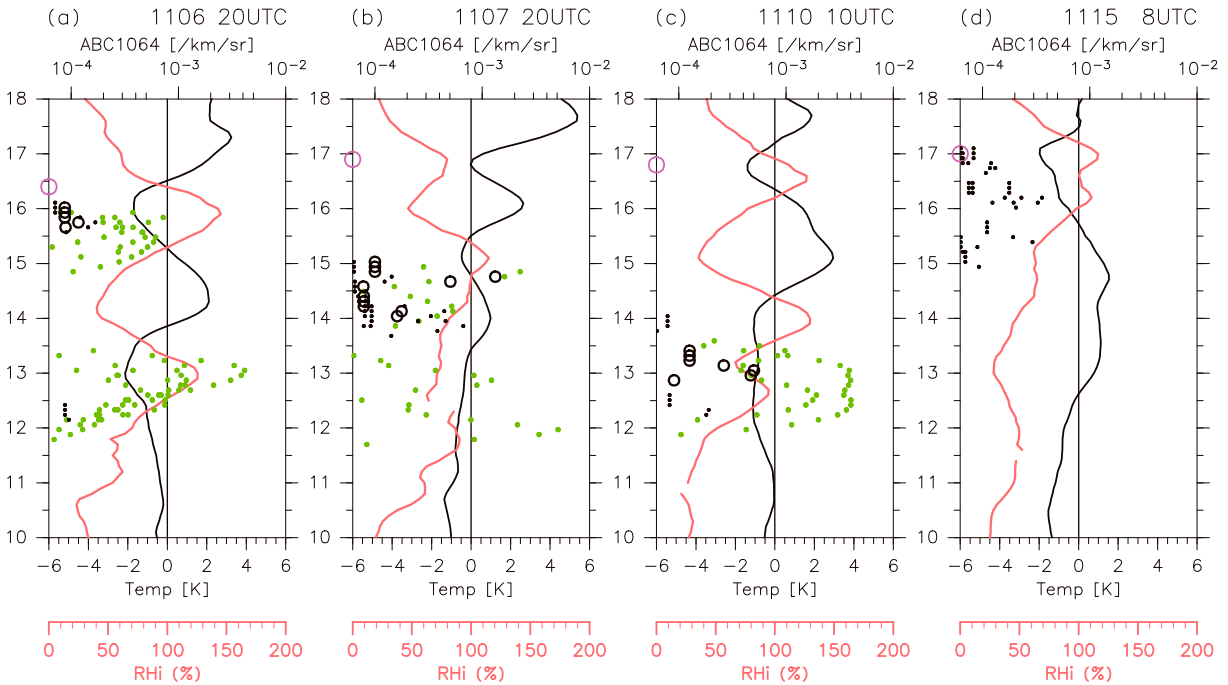


Figure 2. Profiles of temperature anomaly (black lines; in K), relative humidity over ice (red lines; %), and the 1064 nm attenuated backscatter coefficient (green circles for all cirrus and black circles for SVC ($\tau < 0.03$); circles at ± 4 h centered at the time of the CFH launch and larger circles at ± 1 h of the CFH launch time in $\text{km}^{-1} \text{ sr}^{-1}$) at 10–18 km on (a) 20 UTC in 6 November, (b) 20 UTC in 7 November, (c) 10 UTC in 10 November, and (d) 8 UTC in 15 November. The purple circles denote the location of the cold-point tropopause.

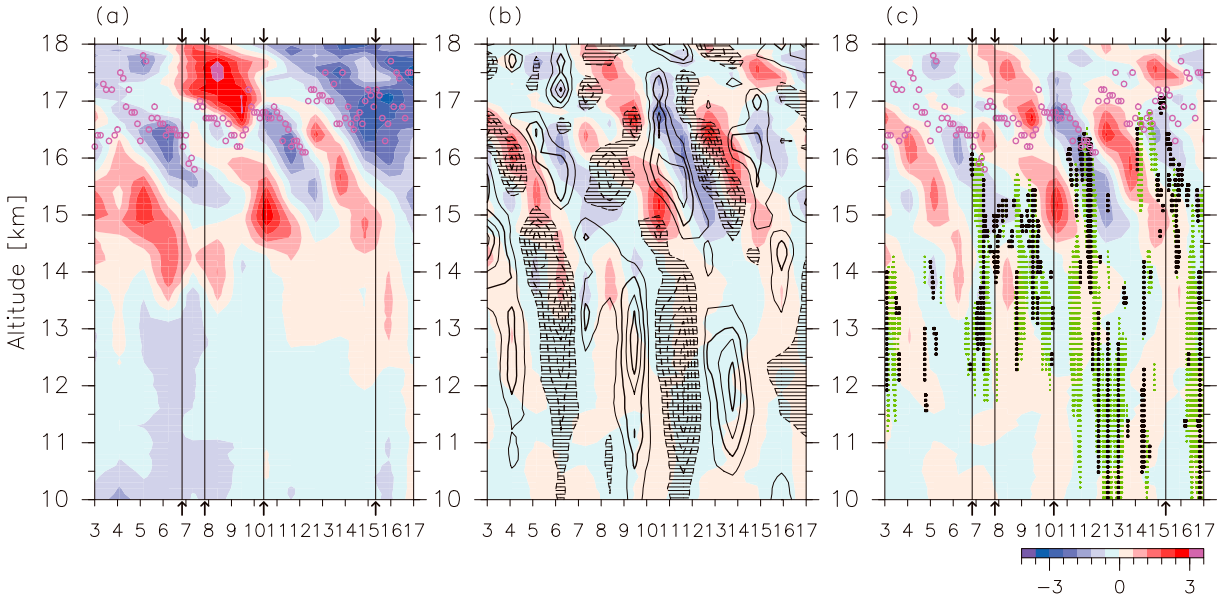


Figure 3. Time-altitude distributions of (a) temperature anomaly (colors; in K), (b) the <7 day filtered temperature (colors; in K) and velocity wind (contours and shading; 1.5 m s^{-1} interval), and (c) temperature anomaly having <7 day periods (colors; in K) and the 1064 nm attenuated backscatter coefficient (green dots for all cirrus and black dots for SVC; regions with $\geq 6.2 \times 10^{-5} \text{ km}^{-1} \text{ sr}^{-1}$) over the R/V *Mirai* at 10–18 km. The purple circles denote the location of the cold-point tropopause. Vertical lines denote the times of the CFH launches corresponding to results shown in Figure 2.

and SVC clouds was high during the period of 3–16 November, as measured over a time scale of several days; therefore, we focus on this period in the following discussion. Note that the backward trajectory and cloud image analyses show that the cirrus variability during 3–16 November was less affected by deep convections (not shown).

[11] Figure 2 shows vertical profiles of relative humidity over ice (RH_i), temperature anomalies, and P_{1064} between 10 km (upper troposphere) and 18 km (upper part of the TTL) in 6, 7, 10, and 15 November. The temporal range for the P_{1064} profiles is ± 4 h centered on the time of the CFH launch. High supersaturation (up to $\sim 150\%$ RH_i) and high RH_i ($>90\%$) were observed between 12 km and the cold-point tropopause. In 6 November, a high supersaturation layer ($\sim 150\%$ RH_i), in which there were large P_{1064} signals, was found at approximately 16 km. Similar cases of high RH_i and significant P_{1064} coexistence were also found on other days (e.g., at ~ 15 km in 7 November, at ~ 13.5 km in 10 November, and at ~ 16 – 17 km in 15 November). The geometric thickness of these layers was equal to or less than 2 km. In 6 November, a high RH_i at 16 km coexisted with a negative temperature anomaly; such an anticorrelation between RH_i and the temperature anomaly was also observed on other days. Colder regions provide favorable conditions for cirrus persistence or formation in situ and via horizontal large-scale transport, whereas warmer regions tend to evaporate cirrus particles. Specifically, to understand the cirrus variability, it is important to clearly identify the type of disturbances that affect the temperature field throughout the TTL. In 7 and 10 November, a cirrus signal was not detected in the P_{1064} data near the cold-point tropopause (~ 16.5 – 17 km) in which the high RH_i and negative temperature anomalies were confirmed; we discuss this cirrus absence later by considering temperature and wind components of large-scale wave structures.

[12] The variability of the dynamical fields measured by the regular radiosounding on the R/V *Mirai* is shown in Figure 3. We observed a wave signal with an amplitude of ~ 1 – 3 K around 15–16 km, with a perturbation time scale of ~ 4 days. There was a substantial meridional wind component with a time scale of ~ 4 days around 15.5 km that corresponded to the temperature oscillations (Figure 3b). To identify waves, Figures 4a and 5a show the propagation direction and the horizontal structure of the two types of equatorial waves, i.e., the $n=0$ eastward inertio-gravity equatorial wave ($n=0$ eastward inertio-gravity (EIG) wave) and the equatorial Kelvin wave, using ERA-Interim 125 hPa data. Figure 4a shows the longitude-time distribution of the total temperature anomaly (<7 day period) and the $n=0$ EIG and equatorial Kelvin wave components with a <7 day period at 125 hPa (~ 15.3 km) and at 7.5°S . We extracted the $n=0$ EIG wave and equatorial Kelvin wave components using filters for the specific wave number-frequency domain; thus, we used zonal wave numbers from 1 to 14, periods from 1.82 to 5 days, and equivalent depths from 8 to 240 m for $n=0$ EIG waves, whereas we used zonal wave numbers from 1 to 10, periods from 4 to 7 days, and equivalent depths from 8 to 240 m for Kelvin waves [Suzuki and Shiotani, 2008; Suzuki et al., 2010b]. Eastward propagating signals were observed in the Eastern Hemisphere. We observed a zero-temperature anomaly in 6–7 November, a warm anomaly in 10 November, and a zero value again in 15 November around the location of the R/V *Mirai*; these observations are consistent with the radiosonde results collected on the vessel (Figures 2 and 3b).

[13] Here linear theory is used to confirm that the <7 day period disturbance around 10 November at ~ 15 – 16 km is the $n=0$ EIG wave; in Figure 3b, the vertical wavelength, λ_z , is estimated as ~ 4 km (the positive region from 14.5 km to 16.5 km in 10 November corresponds to half the vertical

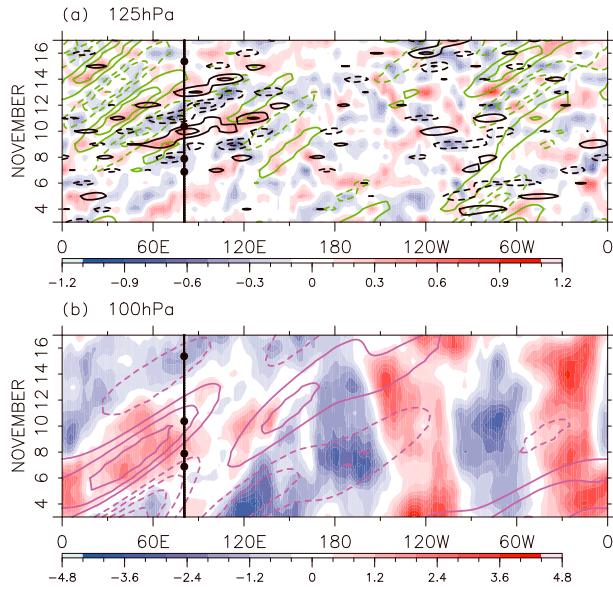


Figure 4. Longitude-time distributions at 7.5°S of (a) temperature anomaly of <7 day periods (colors; in K), $n=0$ eastward moving inertial gravity waves (black contours; 0.2 K interval) and equatorial Kelvin waves having <7 day period components (green contours; 0.2 K interval) at 125 hPa , and (b) temperature anomaly having >7 day periods (purple contours; 0.4 K interval) at 100 hPa . The wave extraction method is described in the text. The black lines indicate the location of the R/V *Mirai*, and the large black dots denote the times of the CFH launches corresponding to the results shown in Figure 2.

wavelength) and the period, T , is estimated as ~ 3.6 day (the positive region from 9 to 11 November at 15.3 km corresponds to half the wavelength). This period corresponds to the inertia period at 8.0°S where the R/V *Mirai* stayed (~ 3.6 days). Additionally, the Brunt-Väisälä frequency (N) and the background zonal wind (U) at the TTL (averaged for $13.5\text{--}16.5\text{ km}$) from 31 October to 28 November were estimated to be $1.4 \times 10^{-2}\text{ s}^{-1}$ and -4.6 m s^{-1} , respectively. Figure 4a shows the warm anomaly moving eastward over the equatorial Indian Ocean from 8 to 12 November at a zonal phase speed (c_x) of $\sim 13\text{ m s}^{-1}$ (which was roughly estimated using the 0.2 K contour line from $\sim 70^{\circ}\text{E}$ at 12 UTC in 8 November to $\sim 80^{\circ}\text{E}$ at 12 UTC in 9 November) with a zonal wavelength (λ_x) of $\sim 25^{\circ}$ longitude (which was roughly estimated using the warm anomaly for one half wavelength in 10 November). These wave parameters are consistent with the linear theory regarding the $n=0$ EIG wave [e.g., Andrews *et al.*, 1987, equation (4.7.16')]. We confirmed that the latitudinal antisymmetric components were dominant, and the temperature and geopotential height peaks were located at $\sim 5^{\circ}\text{N}$ and 5°S around $75^{\circ}\text{E}\text{--}111^{\circ}\text{E}$ at 125 hPa in 11 November using temperature, horizontal wind, and geopotential height anomalies of the <7 day period and eastward propagating component (Figure 5a). The horizontal structure was also consistent with the theoretical structure of the $n=0$ EIG wave (Figure 6). Note that the c_x and λ_x values estimated using the linear equation were $\sim 11\text{ m s}^{-1}$ and $\sim 18^{\circ}$, respectively; these values were similar to the estimated values ($\sim 13\text{ m s}^{-1}$ and $\sim 25^{\circ}$) from Figure 4a.

[14] After 7 November, equatorial Kelvin waves of a <7 day period were observed on the western side of the vessel (Figure 4a). Because the equatorial Kelvin waves of the <7 day period was consistently overlapped with the $n=0$

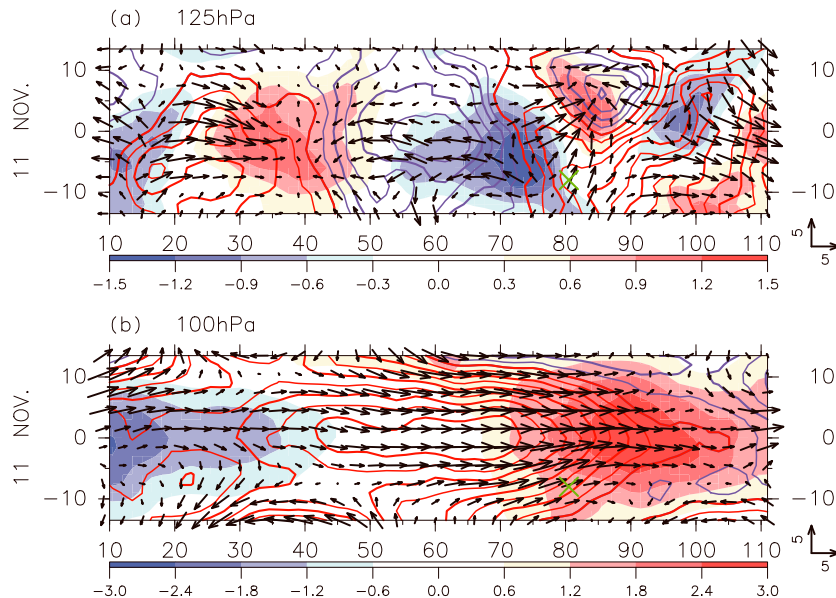


Figure 5. Longitude-latitude distributions of temperature (colors; in K), geopotential height (contours; 1.5 m interval), and horizontal wind components (vectors; m s^{-1}) of (a) a <7 day period and (b) a >7 day period eastward propagating wave in 11 November. Green crosses indicate the location of the R/V *Mirai* (8.0°S , 80.5°E).

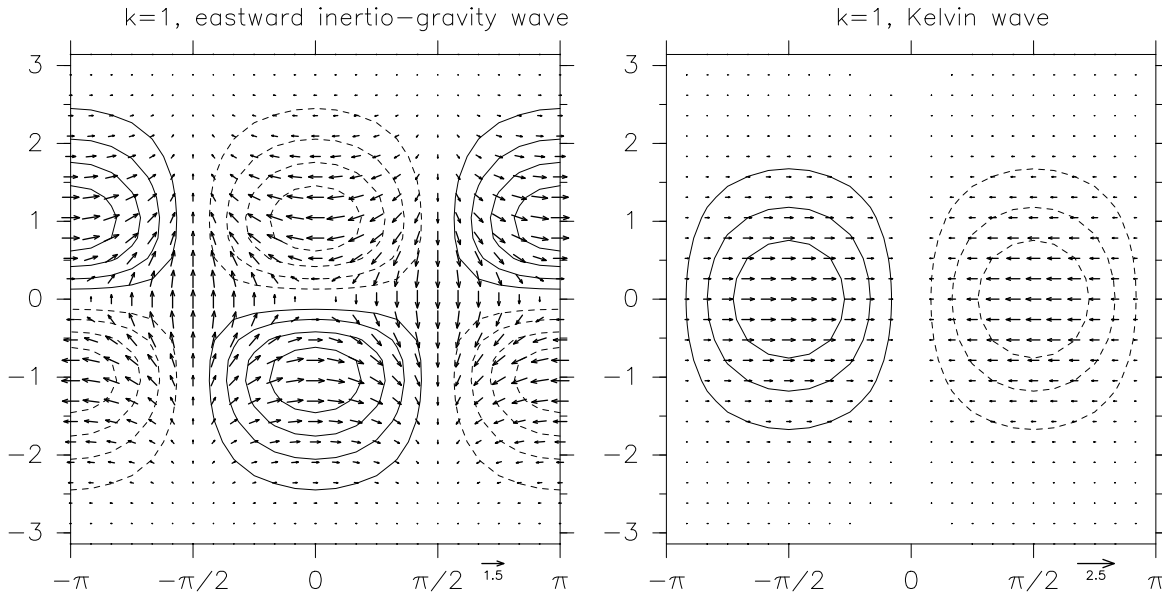


Figure 6. Horizontal structures of a nondimensional zonal wave number $k=1$ for theoretical solutions are shown for (left) $n=0$ eastward inertio-gravity equatorial waves and (right) equatorial Kelvin waves. Vectors denote the horizontal wind component. Contours show the geopotential at intervals of 0.25 arbitrary units. Negative contours are dashed, and the zero contour is omitted.

EIG waves over the R/V *Mirai* during this period, the parameters of the equatorial Kelvin waves of the <7 day period could not be estimated from the linear wave theory using the radiosonde results (Figure 3b). However, we confirmed that the equatorially symmetric features around 20°E – 75°E (Figure 5a) showed the theoretical structure of the equatorial Kelvin waves (Figure 6). Note that the equatorial Kelvin waves around the tropopause observed here had a time period (~ 4 days) similar to those reported by *Holton et al.* [2001], although the equatorial Kelvin waves around the tropopause had an average time period of ~ 9 – 14 days [*Suzuki and Shiotani*, 2008]. We can observe from the above result that cirrus variability in P_{1064} signals was mainly caused by both the ~ 4 day period waves, i.e., the $n=0$ EIG and the equatorial Kelvin wave.

[15] Figure 4b shows the longitude-time distribution of the total temperature anomaly (>7 day period) and the extracted equatorial Kelvin wave with a period longer than 7 days (i.e., zonal wave numbers from 1 to 10, periods from 7 to 23 days, and equivalent depths from 8 to 240 m for the wave number-frequency domain) at 100 hPa (~ 16.5 km) and at 7.5°S . We observed a warm anomaly having a >7 day period and a positive phase of equatorial Kelvin wave over the R/V *Mirai* in 10 November, a weaker warm anomaly having a >7 day period with a zero phase of equatorial Kelvin wave in 7 November, and cold anomalies having a >7 day period and negative phases of equatorial Kelvin waves around 6 November and 15 November. We confirmed that the horizontal structure shows the theoretical equatorial Kelvin wave characteristics (Figure 6; i.e., all components are symmetric about the equator, there is no meridional wind component, and the zonal wind anomaly correlates with the geopotential height anomaly) at 100 hPa and 10°E – 111°E in 11 November using temperature, horizontal wind, and geopotential height anomalies with >7 day period and the eastward propagating component (Figure 5b). We can also confirm that the equatorial Kelvin wave having a >7 day period passed over the

R/V *Mirai* during November based on the radiosonde data; in Figure 3a, the oscillation at 16.5–18 km has a time period of ~ 16 days, which was roughly estimated using the peak to peak in 8 and 16 November. Since the amplitude of 16 day oscillation is significant only in the zonal but not in the meridional wind (not shown), it is tempted to interpret it in terms of equatorial Kelvin wave.

[16] Clouds frequently spread into cold anomalies of equatorial Kelvin waves around the tropical tropopause [*Suzuki et al.*, 2010a]. However, cirrus clouds disappeared due to the warmer anomaly of the ~ 4 day period wave around 16.5 km during 15–16 November despite the cold anomaly of ~ 16 day period Kelvin wave (Figure 3c). On the other hand, although the waves of the ~ 4 day period created favorable temperatures and RH_i conditions for cirrus formation, the cirrus clouds were absent around the cold-point tropopause during 7–11 November (Figure 2). This is because this period corresponds to the transition from the cold phase to the warm phase (shown in Figure 3a around the descending zero-temperature anomaly from ~ 17 km in 7 November to ~ 16.5 km in 10 November) which is the maximum downward wind (subsidence) region of the theoretical equatorial Kelvin waves. Under these conditions, it is difficult to produce and maintain cirrus clouds. Furthermore, it is likely that cirrus clouds disappeared under unfavorable conditions (e.g., downward flow and dry) caused by the ~ 4 day waves, although the ~ 16 day wave was producing favorable conditions.

4. Conclusions

[17] Cirrus cloud variability associated with $n=0$ EIG waves and equatorial Kelvin waves having a ~ 4 day period and with another equatorial Kelvin wave having a ~ 16 day period were observed over the tropical Indian Ocean in November of 2011. The occurrence of this cirrus cloud variability coincided with the occurrence of high supersaturation

(up to ~150% RH_i) and high relative humidity with respect to ice (>90%) primarily associated with temperature disturbances caused by the two types of equatorial waves having a ~4 day period between 12 km and the cold-point tropopause. This study has shown for the first time a case in which the cirrus variability is affected by $n=0$ EIG waves with relatively small amplitude (1–3 K), although this wave mode is not dominant around the TTL [Tindall *et al.*, 2006]. Cirrus clouds disappear in a warmer anomaly of a ~4 day period wave even when there is a cold anomaly of a ~16 day period Kelvin wave. Thus, it is suggested that cirrus clouds disappear under unfavorable conditions caused by a shorter-period (small-scale) wave even when favorable conditions are produced by another longer-period (large-scale) wave, such as the equatorial Kelvin waves as reported by previous studies [Immler *et al.*, 2008; Suzuki *et al.*, 2010a]. However, when a warm phase of longer-period (~16 days) equatorial Kelvin waves propagates around the tropopause, the cirrus clouds are absent around the cold-point tropopause even when short-period waves cause favorable temperature and RH_i conditions for cirrus formation.

[18] **Acknowledgments.** We express our sincere thanks to the technical staff of Global Ocean Development Inc. for their observation support on board the R/V *Mirai*. We also thank N. Nishi of Kyoto University, S. Ogino of Japan Agency for Marine-Earth Science and Technology, and S. Iwasaki of National Defense Academy of Japan for their helpful discussions. This work was supported by KAKENHI (23540512). The GFD-DENNOU Library was used for drawing figures.

References

- Andrews, D. G., J. R. Holton, and C. B. Leovy (1987), *Middle Atmosphere Dynamics*, 489 pp., Academic, San Diego, Calif.
- Boehm, M. T., and J. Verlinde (2000), Stratospheric influence on upper tropospheric tropical cirrus, *Geophys. Res. Lett.*, *27*, 3209–3212, doi:10.1029/2000GL011678.
- Dee, D. P., et al. (2011), The ERA-Interim reanalysis: Configuration and performance of the data assimilation system, *Q. J. R. Meteorol. Soc.*, *137*, 553–597, doi:10.1002/qj.828.
- Eguchi, N., and M. Shiotani (2004), Intraseasonal variations of water vapor and cirrus clouds in the tropical upper troposphere, *J. Geophys. Res.*, *109*, D12106, doi:10.1029/2003JD004314.
- Fueglistaler, S., A. E. Dessler, T. J. Dunkerton, I. Folkins, Q. Fu, and P. W. Mote (2009), Tropical tropopause layer, *Rev. Geophys.*, *47*, RG1004, doi:10.1029/2008RG000267.
- Fujiwara, M., et al. (2009), Cirrus observations in the tropical tropopause layer over the western Pacific, *J. Geophys. Res.*, *114*, D09304, doi:10.1029/2008JD011040.
- Holton, J. R., and A. Gettelman (2001), Horizontal transport and the dehydration of the stratosphere, *Geophys. Res. Lett.*, *28*(14), 2799–2802, doi:10.1029/2001GL013148.
- Holton, J. R., M. J. Alexander, and M. T. Boehm (2001), Evidence for short vertical wavelength Kelvin waves in the Department of Energy-Atmospheric Radiation Measurement Nauru99 radiosonde data, *J. Geophys. Res.*, *106*(D17), 20,125–20,129, doi:10.1029/2001JD900108.
- Immler, F., K. Kruger, M. Fujiwara, G. Verver, M. Rex, and O. Schrems (2008), Correlation between equatorial Kelvin waves and the occurrence of extremely thin ice clouds at the tropical tropopause, *Atmos. Chem. Phys.*, *8*, 4019–4026.
- Inai, Y., T. Shibata, M. Fujiwara, F. Hasebe, and H. Vömel (2012), High supersaturation inside cirrus in well-developed tropical tropopause layer over Indonesia, *Geophys. Res. Lett.*, *39*, L20811, doi:10.1029/2012GL053638.
- Jensen, E., and L. Pfister (2004), Transport and freeze-drying in the tropical tropopause layer, *J. Geophys. Res.*, *109*, D02207, doi:10.1029/2003JD004022.
- Kärcher, B. (2002), Properties of subvisible cirrus clouds formed by homogeneous freezing, *Atmos. Chem. Phys.*, *2*, 161–170, doi:10.5194/acp-2-161-2002.
- Martins, E., V. Noel, and H. Chepfer (2011), Properties of cirrus and subvisible cirrus from nighttime Cloud-Aerosol Lidar with Orthogonal Polarization (CALIOP), related to atmospheric dynamics and water vapor, *J. Geophys. Res.*, *116*, D02208, doi:10.1029/2010JD014519.
- Matsuno, T. (1966), Quasi-geostrophic motions in the equatorial area, *J. Meteorol. Soc. Jpn.*, *44*(1), 25–43.
- Nishizawa, T., N. Sugimoto, and I. Matsui (2010), Development of a dual-wavelength high-spectral-resolution lidar, Proc. SPIE 7860, Lidar Remote Sensing for Environmental Monitoring XI, 78600D (November 11, 2010); doi:10.1117/12.870068.
- Nishizawa, T., N. Sugimoto, I. Matsui, and T. Takano (2012), Development of two-wavelength high-spectral-resolution lidar and application to shipborne measurements, Reviewed and revised papers presented at the 26th International Laser Radar Conference, pp. 151–154.
- Pfister, L., et al. (2001), Aircraft observations of thin cirrus clouds near the tropical tropopause, *J. Geophys. Res.*, *106*, 9765–9786.
- Sassen, K., and B. S. Cho (1992), Subvisual-thin cirrus lidar dataset for satellite verification and climatological research, *J. Appl. Meteorol.*, *31*, 1275–1285, doi:10.1175/1520-0450(1992)031<1275:STCLDF>2.0.CO;2.
- Solomon, S., K. H. Rosenlof, R. W. Portmann, J. S. Daniel, S. M. Davis, T. J. Sanford, and G.-K. Plattner (2010), Contributions of stratospheric water vapor to decadal changes in the rate of global warming, *Science*, *327*, 1219–1223, doi:10.1126/science.1182488.
- Suzuki, J., and M. Shiotani (2008), Space-time variability of equatorial Kelvin waves and intraseasonal oscillations around the tropical tropopause, *J. Geophys. Res.*, *113*, D16110, doi:10.1029/2007JD009456.
- Suzuki, J., M. Fujiwara, A. Hamada, Y. Inai, J. Yamaguchi, R. Shirooka, F. Hasebe, and T. Takano (2010a), Cloud-top height variability associated with equatorial Kelvin waves in the tropical tropopause layer during the Mirai Indian Ocean cruise for the Study of MJO-convection Onset (MISMO) campaign, *Sci. Online Lett. Atmos.*, *6*, 97–100, doi:10.2151/sola.2010-025.
- Suzuki, J., M. Shiotani, and N. Nishi (2010b), Lifetime and longitudinal variability of equatorial Kelvin waves around the tropical tropopause region, *J. Geophys. Res.*, *115*, D03103, doi:10.1029/2009JD012261.
- Tindall, J. C., J. Thuburn, and E. J. Highwood (2006), Equatorial waves in the lower stratosphere. II: Annual and interannual variability, *Q. J. R. Meteorol. Soc.*, *132*, 195–212, doi:10.1256/qj.04.153.
- Virts, K. S., J. M. Wallace, Q. Fu, and T. P. Ackerman (2010), Tropical tropopause transition layer cirrus as represented by CALIPSO lidar observations, *J. Atmos. Sci.*, *67*, 3113–3129, doi:10.1175/2010JAS3413.1.
- Vömel, H., D. David, and K. Smith (2007), Accuracy of tropospheric and stratospheric water vapor measurements by the cryogenic frost point hygrometer: Instrumental details and observations, *J. Geophys. Res.*, *112*, D08305, doi:10.1029/2006JD007224.
- Wheeler, M., and H. Hendon (2004), An all-season real-time multivariate MJO index: Development of an index for monitoring and prediction, *Mon. Weather Rev.*, *132*, 1917–1932.
- Yoneyama, K., C. Zhang, and C. N. Long (2013), Tracking pulses of the Madden-Julian Oscillation, *Bull. Amer. Meteor. Soc.*, doi:10.1175/BAMS-D-12-00157.1, in press.